Additive Manufacturing 38 (2021) 101774

Contents lists available at ScienceDirect

Additive Manufacturing

journal homepage: www.elsevier.com/locate/addma

Research Paper

# *In-situ* synthesis of Metal Organic Frameworks (MOFs)-PA12 powders and their laser sintering into hierarchical porous lattice structures

Binling Chen *, Richard Davies, Hong Chang, Yongde Xia, Yanqiu Zhu, Oana Ghita

*College of Engineering, Mathematics and Physical Sciences, University of Exeter, Exeter EX4 4QF, UK*

ARTICLE INFO

*Keywords:*
Metal organic frameworks
Nanocomposites
Laser sintering
3D printing
$CO_2$ adsorption

ABSTRACT

This paper demonstrates the utilisation of in-situ synthesised novel metal organic framework (MOF)-polymer nanocomposite laser-sintered parts with enhanced $CO_2$ adsorption properties. Making use of polyamide PA12, one of the most common materials in powder bed fusion process as the base polymer, an in-situ synthesis of nanofiller ZIF-67 crystals on the surface of polyamide polymer particles was proposed to allow the fabrication of a nanocomposite powder with a good dispersion, reducing any health and safety handling issue arising from use of loose nanoparticles. This in-situ synthesis method allowed a maximum exposure of the ZIF-67 nano-porous sites. Laser sintering was used to fabricate porous structures with additional macro-pores and controlled cavities to increase the surface area. The laser-sintered ZIF67-PA12 part at only 2.6% wt ZIF-67 concentration exhibited a $CO_2$ capacity of 3.02 and 4.89 $cm^3/g$ at 298 K and 273 K at 1 bar. This in-situ synthesis method of making ZIF67-PA12 powders combined with the design freedom and the ease of fabrication of parts opens opportunities in a wider range of applications for MOFs such as energy storage and conversion.

## 1. Introduction

Additive Manufacturing (AM), also known as 3D Printing, has expanded significantly over the last couple of decades across many sectors due to a number of key advantages that traditional manufacturing cannot offer: geometrical complexity, tool-less manufacture and sustainable manufacturing. Current polymeric AM covers a wide range of technologies such as Freeform Form Fabrication (FFF), Powder Bed Fusion (PBF), Direct Ink Writing (DIW) and photo-polymerization (stereolithography) [1].

A significant part of polymeric AM research is focused on the development of polymers for improved mechanical performance [2–6]. The use of AM for functionality such as carbon capture and gas storage devices [7,8], solar cells and photocatalytic reactors [9,10], and electrochemical energy storage devices (eg. lithium-ion batteries and supercapacitors) [11,12], has received little attention and has seen little development [13–16].

The family of metal organic frameworks (MOFs) is one of the most exciting and fast-developing group of organic-inorganic hybrid nanomaterials that have been studied in the last decade due to their great versatility in chemistry with a large variety of porous structures applicable in various temperature ranges and solvent types [17,18]. MOFs are typically crystalline solids. Many energy applications will benefit if the MOFs could be anchored onto a proper support without damaging their unique properties. As a special family of MOFs, the zeolitic imidazolate frameworks (ZIFs) consist of transition metal cations and imidazolate ligands with a well-defined and tunable morphology [19]. For example, ZIF-67 consists of metal ions $Co^{2+}$ and organic ligand 2-Methylimidazole (MIM). The $Co^{2+}$ coordinating clusters, also known as secondary building units, are linked with MIM to form a unit cell. Its structure has a cubic crystal symmetry [20]. Thanks to its abundant active sites and highly stable structure (i.e. degradation starts at 420 °C in nitrogen), ZIF-67 has been studied for many applications, including catalysis, gas adsorption, molecular separation and so on [20].

In order to uncover MOFs' potential, various AM techniques have recently been tried for building MOF-enhanced polymeric composite components, in the hope that the AM processing could result in added benefits of desired shape and geometry, enlarged surface area, and enhanced porosity for the support polymer, hence improved component performance. As such, Freeform Form Fabrication has been applied to fabricate MOF-polymer devices [21,22]. For example, 1%, 5% and 10% MOF-5 and acrylonitrile butadiene styrene (ABS) were first solvent cast, melt compounded, and then extruded to form filament feeding materials. The obtained filament was used for printing parts for hydrogen

* Corresponding author.
*E-mail address:* B.Chen@exeter.ac.uk (B. Chen).

https://doi.org/10.1016/j.addma.2020.101774
Received 17 August 2020; Received in revised form 30 November 2020; Accepted 8 December 2020
Available online 14 December 2020

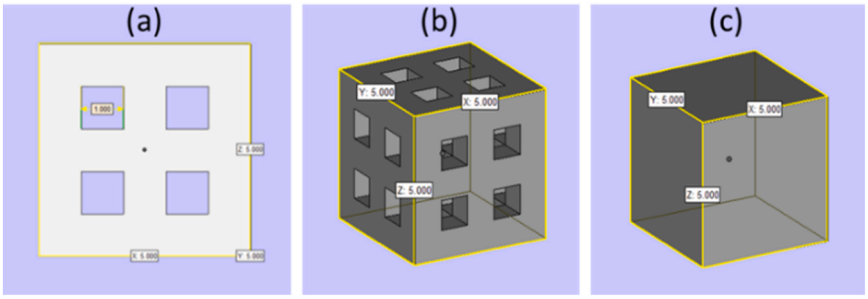


**Fig. 1.** CAD models of laser sintered samples (a-b) porous lattice structure (c) solid structure using 2%ZIF67-PA12 powder.

($H_2$) storage application [21]. The $H_2$ capacity of printed material ABS-10%MOF-5 was measured to be only 1.15 times higher than that of the pure ABS. The approach has some limitations as the dispersion of MOF-5 into the ABS matrix might not be uniform and the majority of the pores in MOF-5 could be blocked due to the nanomaterial's encapsulation into the molten polymer. The SEM cross-section images of the printed part confirmed that although some of MOF-5 crystals are visible, a significant amount is embedded into the ABS matrix.

Other studies have reported using direct ink writing to fabricate porous structured MOFs-based parts [23,24]. However, in the studies, MOFs fillers and polymer were mechanically mixed to form inks before printing. The dispersion of MOFs in the polymer matrix is concerned, as mechanical mixing generally lead to the nanofiller agglomeration, and thus weaken the parts performance.

Powder Bed Fusion process is an alternative AM method to Freeform Form Fabrication technology which allows fabrication of MOF-polymer parts [25,26]. Recently, Lahtinen et al. reported using a dry-mix powder of 10 wt% MOF copper (II) benzene-1,3,5-tricarboxylate (HKUST-1) and PA12. This mixed powder was laser sintered to form solid disks for $CO_2$ adsorption application [25]. Based on a TG/DSC analyser, the $CO_2$ flow results showed that $CO_2$ increased roughly 0.6 wt% and 6 wt% for the printed part containing 10 wt% HKUST-1 and the bulk HKUST-1 powder, respectively. It seems that the dry-mix powder preparation method and laser sintering process did not negatively affect the activity of the HKUST-1. However, one should consider the results carefully, since TG/DSC analyzer is a bulk $CO_2$ capacity measurement and the as-printed solid disk structure obviously blocks the HKUST-1 crystals into the PA12 matrix. In addition, this dry-mix powder preparation method cannot achieve uniform nanofiller dispersion, and the handling of nanoparticles needs to be considered at a larger scale.

In the present study, for the first time, an in-situ hydrothermal synthesis method has been applied to form directly ZIF67-PA12 nanocomposite powders, where ZIF-67 crystals grow uniformly on the surface of PA12 polymeric particle. ZIF-67 was selected in this study due to its ability to adsorb $CO_2$ molecules and facile synthesis method to be prepared [20,27]. The paper considers particle size distribution and flowability of the new ZIF67-PA12 powders to confirm their processability in powder bed fusion process. Functional parts with a porous structure have been successfully laser sintered by using the prepared feedstock materials. $CO_2$ adsorption performance of laser-sintered porous parts has been measured. The laser sintered porous lattice structure containing 2.6 wt% ZIF-67 crystals, achieved a $CO_2$ adsorption capacity of 3.02 $cm^3/g$ at 298 K and 1 bar, a superior $CO_2$ adsorption performance when compared to literature [25].

## 2. Experimental

### 2.1. Materials

The commercial laser sintering grade PA2200 (Polyamide 12, PA12, or Nylon12) powder (Mw = 29,000) was purchased from EOS Gmbh; 2-Methylimidazole (MIM) and cobalt nitrate hexahydrate (Co$(NO_3)_2{\cdot}6H_2O$) were purchased from Sigma-Aldrich.

### 2.2. Material preparation

2-Methylimidazole (MIM) was first dissolved in 1.5 L distilled water. 500 g of PA12 powder (PA2200) was then added into that MIM aqueous solution. The solution was gently mixed. Cobalt nitrate hexahydrate was added upon continuous mixing for 24 h. The final powders were collected using filtering, washing followed by drying in the oven at 80 °C overnight.

The method to synthesis ZIF-67 is based on previous study [28,29]. The study calculated a synthesis yield of 66% which in equated to a theoretical value of 0.1, 1 and 2 wt% of ZIF-67 into PA12 powder, referred as 0.1%ZIF67-PA12, 1%ZIF67-PA12, and 2%ZIF67-PA12, respectively. For comparison, 2 wt% ZIF67 was dry mixed with PA12 powder and used as a reference sample, referred to as 2%ZIF67-PA12 dry-mix powder.

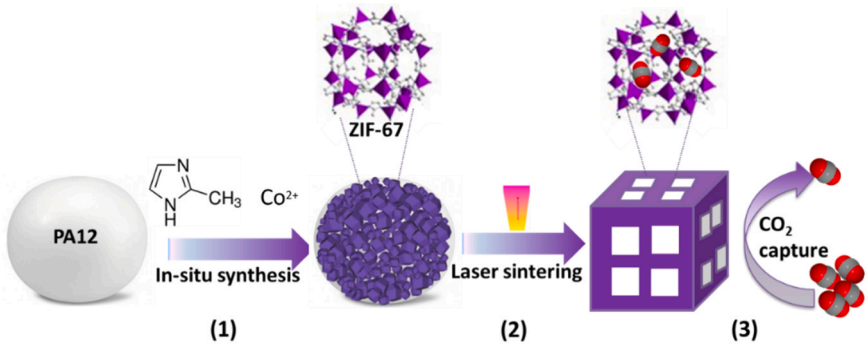


**Fig. 2.** Schematic diagram of (1) the preparation of ZIF67-PA12 nanocomposite powders; (2) laser sintering of the prepared powders into porous part; (3) $CO_2$ capture application of laser-sintered part.

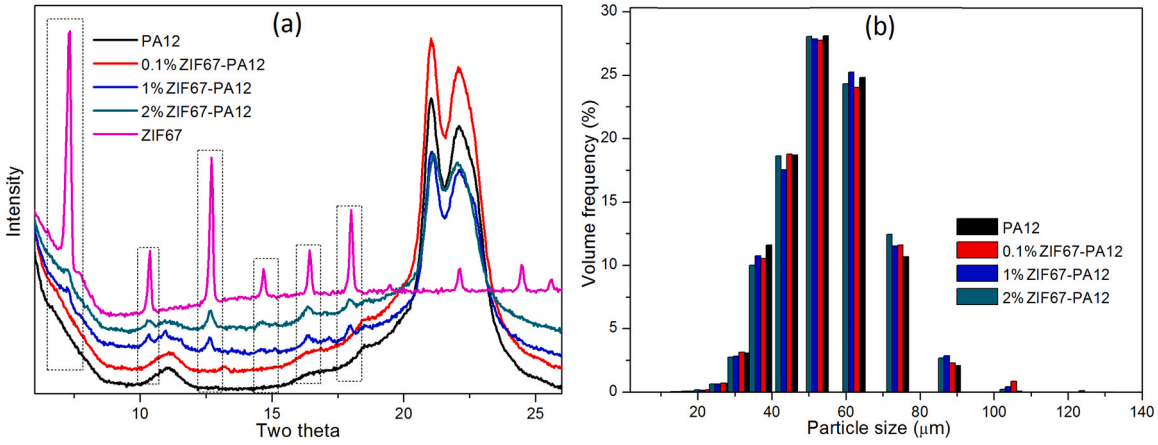


**Fig. 3.** (a) XRD patterns and (b) particle size distributions of the as-synthesised ZIF67-PA12 nanocomposites.

### 2.3. Powder bed fusion process

A Sharebot Snowwhite system using a $CO_2$ laser was applied to laser sinter the prepared powders. The process parameters were set at 4.2 W power, 2400 mm/s laser speed, the hatching distance is 0.1 mm and the process temperature is 185 °C with 20 warming layers. Energy density was calculated to be 0.018 J/mm$^2$.

It is known that the AM process has the ability to create complex structures, intricate internal features with internal cavities through design and manufacture and to fabricate macro-porous structures by controlling the manufacturing settings. Low energy density values would lead to more porous structures. Here we took advantages of these unique characteristics of the laser sintering process to enhance further the porosity by keeping the ZIF-67 crystals exposed on the surface of PA12 and increasing the surface area through design. Solid 5 mm * 5 mm * 5 mm cubes and porous lattice cubes were created in CAD and then laser sintered as shown in Fig. 1.

### 2.4. Double coating process

A dip coating method was also used to increase the amount of ZIF-67 crystals on the surface of laser sintered 2%ZIF67-PA12 porous part. The laser sintered 2%ZIF67-PA12 porous part was dipped into a solvent containing MIM and cobalt nitrate for ZIF-67 coating. After 3 h, the dipped part was taken out for dry.

### 2.5. Overall manufacturing process

Fig. 2 describes the entire process from powder functionalization through to part formation. It covers: (1) in-situ synthesis of nanocomposite powders; (2) laser sintering of powders with porous structure; and (3) $CO_2$ capture performance of laser-sintered part.

### 2.6. Material characterisation

#### 2.6.1. Powder analysis

The particle size distribution (PSD) of powders was measured using a Microtrac Sync analyser. The particle size was determined by the intensity of scattered light. Around 4000–6000 particles were captured and analysed in each measurement. Three measurements were repeated for each material.

A Freeman FT-4 powder rheometer was used to assess powder flow properties. Dynamic properties such as Basic Flow Energy (BFE), Specific Energy (SE) and Stability Index (SI) were obtained from the combined stability and variable flow rate test. BFE was measured during the downward blade movement. It provides information of flowability, regarding the difficulty of displacing the powder. The SE was measured by lifting the powder from the bottom of the vessel to the top in an unconfined state. In addition, the bulk property Conditioned Bulk Density (CBD) was obtained from the split mass after conditioning divided by sample volume.

#### 2.6.2. X-ray diffraction (XRD)

X-ray diffraction (XRD) patterns of powdered samples were recorded with a Cu Kα radiation (40 kV-40 mA) at a step time of 1 s and a step size of 0.02°.

#### 2.6.3. Thermal analysis

Thermogravimetric analysis (TGA) was performed using a Mettler Toledo TGA/DSC1 STARe system. Samples were heated from room temperature to 800 °C under a continuous nitrogen flow at a rate of 100 ml min$^{-1}$. Differential scanning calorimetry (DSC) was carried out using a Mettler Toledo DSC 1 STARe system to measure melting, crystallisation and glass transition temperatures. Nitrogen with a flow rate of 50 ml min$^{-1}$ was used during the measurement process. The samples were heated in DSC from 25 °C to 250 °C with a heating rate of 10 °C min$^{-1}$, and then cooled from 250 °C to 25 °C with a heating rate of 10 °C min$^{-1}$. Three repeats of each sample were carried out. The evaluation of the thermal properties has been analysed by using the STARe package software.

#### 2.6.4. Scanning electron microscopy (SEM)

SEM images were recorded using a Nova Nanolab 600 scanning electron microscope in a high vacuum mode, at an acceleration voltage of 20 kV. Both powders and printed samples were coated with a 10 nm-thick Au layer before taking SEM.

#### 2.6.5. Surface area of prepared powders

Surface area of powders were measured by a Quantachrome Autosorb-iQ gas sorptometer and calculated via Brunauer-Emmett-Teller (BET) method based on adsorption data in the partial pressure (P/Po) range of 0.05–0.20. The total pore volume was determined from the amount of nitrogen adsorbed at P/Po of ca. 0.99.

#### 2.6.6. Micro-CT

Micro-CT was applied to investigate the 3D structure of the laser-sintered parts. 2%ZIF67-PA12 porous part was scanned using X-Tek Bench top CT 160 Xi (X-Tek Systems Ltd/Nikon Metrology UK Ltd, England) with a voltage of 65 kV, current of 75 μA, exposure time of 354 ms, 1200 projection and 360° rotation. The CT data was then analysed by using VGStudioMAX software.

#### 2.6.7. Compressive test

Compressive testing experiments of PA12 solid part and 2ZIF67-

**Table 1**
The PSD characteristic parameters of plain PA12 and as-synthesised ZIF67-PA12 nanocomposites.

| | D10 (μm) | D50 (μm) | D90 (μm) |
|---|---|---|---|
| PA12 | 41.31 ± 0.24 | 57.10 ± 0.16 | 79.27 ± 0.20 |
| 0.1%ZIF67-PA12 | 41.23 ± 0.12 | 57.13 ± 0.03 | 79.35 ± 0.08 |
| 1%ZIF67-PA12 | 41.39 ± 0.10 | 57.25 ± 0.08 | 79.39 ± 0.29 |
| 2%ZIF67-PA12 | 42.11 ± 0.17 | 57.88 ± 0.14 | 79.93 ± 0.24 |

PA12 solid part were performed using a LLOYD instrument EZ20 mechanical testing machine at room temperature. The dimension of the compression test specimens is 5 mm * 5 mm * 5 mm. The testing speed was 0.2 mm $min^{-1}$ and the compress depth was set as 4 mm. The stress (MPa) and compressive strain (%) were then evaluated.

#### 2.6.8. $CO_2$ adsorption test

$CO_2$ gas adsorption capacities were investigated on a Quantachrome Autosorb-iQ gas sorptometer by using the conventional static volumetric technique. Prior to the gas adsorption analysis, the samples were evacuated at 120 °C for 2 h under vacuum, then the $CO_2$ uptake measurements were carried out at 0 and 25 °C (273 and 298 K).

## 3. Results and discussion

### 3.1. Characterisation of PA12 and ZIF67-PA12 powders

The crystalline structure of MOFs on the surface of PA12 powders was measured by XRD (shown in Fig. 3a). The XRD pattern of the synthesised ZIF-67 shows the typical peaks of ZIF-67, which are consistent to the literature [28]. Its narrow and strong peaks also indicate the high crystallinity of ZIF-67. Apart from the 0.1%ZIF67-PA12, other ZIF67-PA12 powders have the same XRD peaks as ZIF-67, which means ZIF-67 crystals have been formed through the in-situ method. No obvious XRD patterns of ZIF-67 were observed from the powder 0.1% ZIF67-PA12, this is probably due to the small amount of ZIF-67 (0.1 wt %) in the sample. As a result, XRD patterns confirm the successful formation of ZIF-67 crystals in ZIF67-PA12 powders, without the damage of PA12 crystalline structures that show characteristic XRD peaks in the 2θ range of 20–23°. Fig. 3b shows the particle size distribution (PSD) of the plain PA12 and ZIF67-PA12 powders, and Table 1 provides their PSD characteristic parameters. A slight increase of approx. 0.6–0.7 μm in the PSD results were found between each grade of powders. It can be concluded that synthesis process of ZIF67-PA12 powders has a negligible influence on the PSD.

The SEM helps to observe the morphology of the prepared powders. Fig. 4a and b show the SEM images of plain PA12 powders. The surface of the PA12 particles is not very smooth which can influence the growth of the ZIF-67 crystals. For 0.1%ZIF67-PA12, the shape of ZIF-67 crystals appears to be cubic; ZIF-67 does not cover the whole surface of PA12 (Fig. S1). In the case of 1%ZIF67-PA12, the shape of ZIF-67 crystals is irregular and the size of ZIF-67 crystals becomes larger, but still cannot cover the whole PA12 surface (Fig. S2). While for 2%ZIF67-PA12, the ZIF-67 crystals nearly cover the whole PA12 particle surface (Fig. 4c and d). The energy-dispersive X-ray spectroscopy (EDS) of 2%ZIF-67-PA12 shows a good dispersion of the ZIF-67 crystals (Fig. 5). These SEM images confirm that ZIF-67 crystals have been successfully grown on the surface of PA12 particles in all ZIF67-PA12 samples.

DSC was used to identify any changes in the process temperature induced by the presence of the ZIF-67 [30]. The DSC curves of plain

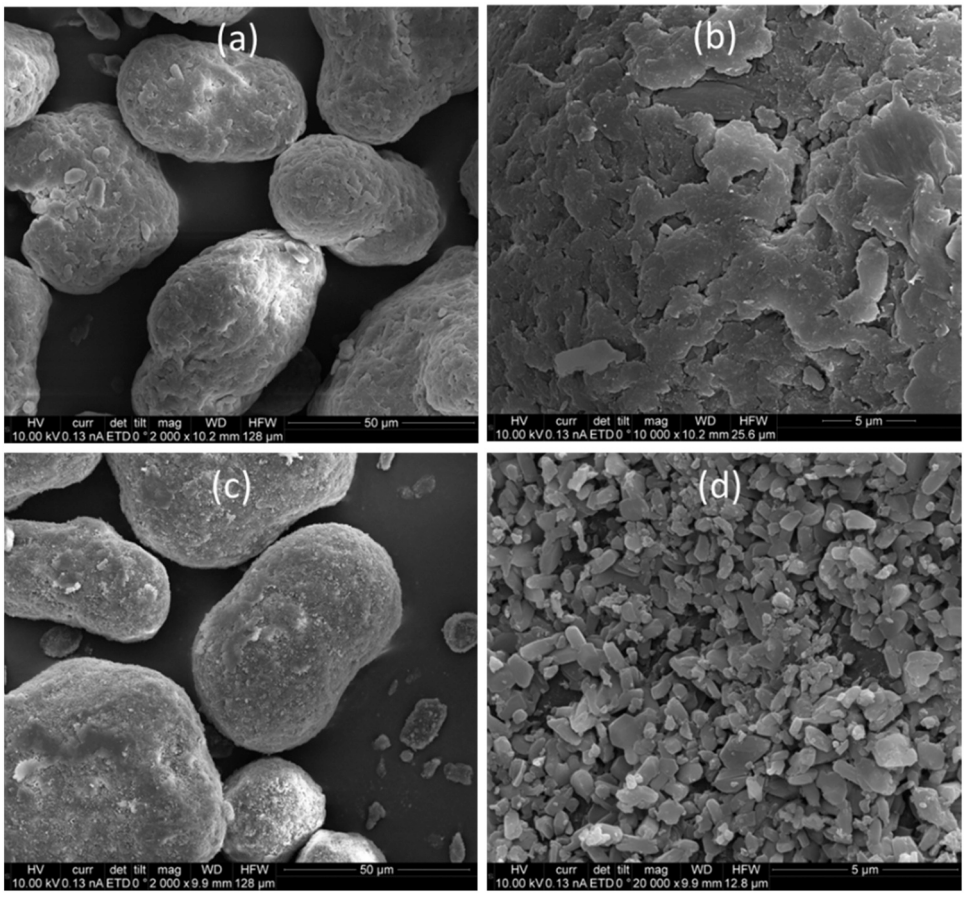


**Fig. 4.** SEM images of (a-b) plain PA12 powder, and (c-d) 2%ZIF67-PA12 powder. Fig. 4d shows a uniform and a high level of the ZIF-67 crystals being formed on the surface of PA12 particles.

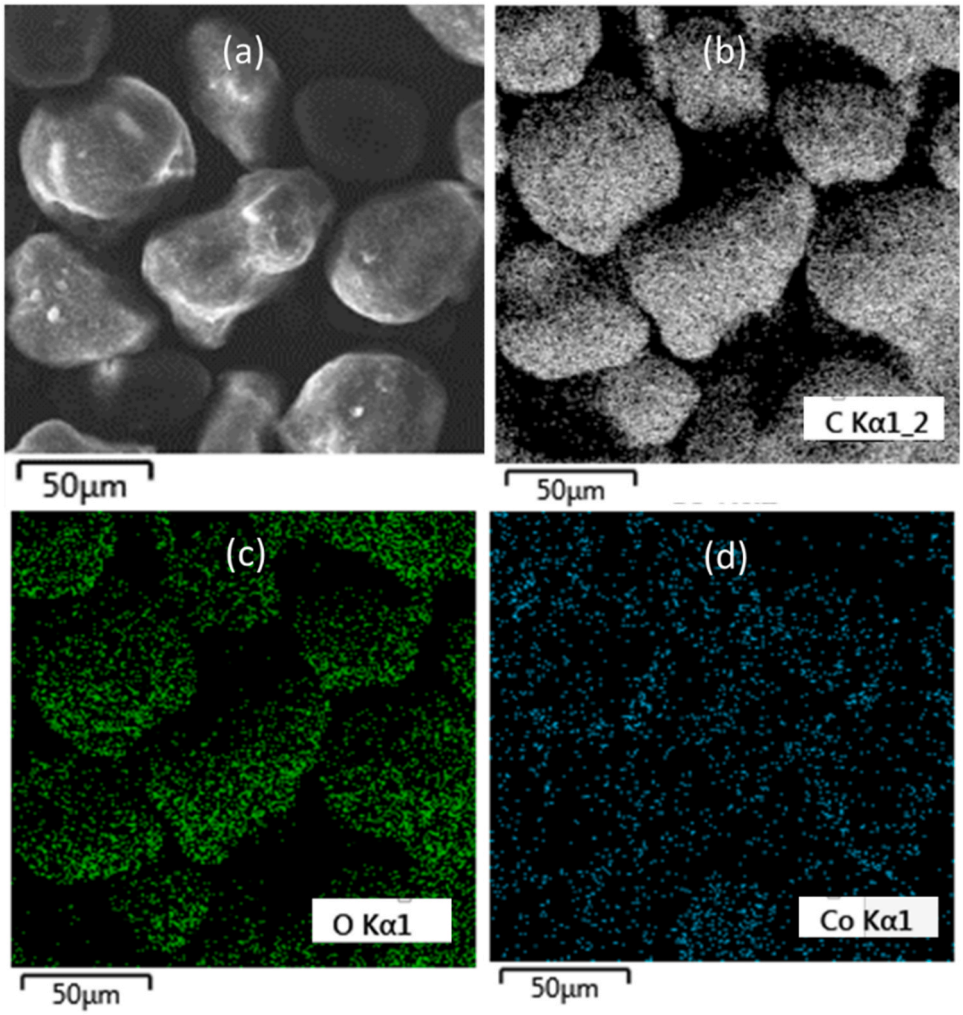


**Fig. 5.** (a) Energy-dispersive X-ray spectroscopy of 2%ZIF67-PA12 powder, with its elemental mapping of (b) C, (c) O and (d) Co element.

PA12 and ZIF67-PA12 powders are shown in Fig. 6a and their onset melting and onset crystallisation temperatures are listed in Table 2. The super-cooling window for laser sintering is a temperature range between the onset melting and onset crystallisation temperature. All the ZIF67-PA12 powders displayed a narrower super-cooling window in comparison with the plain PA12 powder. The crystallisation temperature of the 0.1%ZIF67-PA12, 1%ZIF67-PA12, and 2%ZIF67-PA12 powder are changeable to plain PA12, suggesting that ZIF-67 crystals affect the PA12 crystallisation. Fig. 6b shows the % crystallisation over time for plain PA12 and ZIF67-PA12 powders. It can be found that a lower loading of ZIF-67 (0.1%ZIF67-PA12 and 1%ZIF67-PA12) speeds up the crystallisation rate; while a higher loading of ZIF-67 (2%ZIF67-PA12) slows down the crystallisation rate. ZIF-67 crystals in low amount plays as a nucleation point to facilitate polymer crystallisation, while ZIF-67 crystals in high amount could retard the diffusion and rearrangement of the PA polymer chains, therefore leading to the decrease of crystallisation. This observation is important for the powder bed fusion process. The lower crystallisation rate is beneficial for laser sintering, because it is helpful to the adhesion between each laser sintered layer and it could also reduce the layer curling under the powder bed temperature during the process.

TGA is used to determine the thermal stability of ZIF67-PA12 powders. As shown in Fig. 6c inset, all powders are thermally stable with a slight loss of weight between 25 and 200 °C possibly induced by the drying of composite powder, suggesting that the ZIF67-PA12 powder is suitable for powder bed fusion process. When plotting the 1st derivative of the TGA thermograms of 2%ZIF67-PA12 and reference 2%ZIF67-PA12 dry-mix powders (shown in Fig. 6d), it was noticed that the peak of the in-situ synthesised 2%ZIF67-PA12 is 13 °C higher than that of the dry-mix powder, suggesting that the in-situ synthesised 2%ZIF67-PA12 powder is more stable than the plain polymer itself. This could be the result of some chemical interactions between ZIF-67 crystals and PA12 particle. The AFM nano-mechanical scratch test (Fig. S3) revealed a force of 1.5–3.0 μN required for removing ZIF-67 crystals from the surface of PA12 particles, suggesting the presence of strong interaction between ZIF-67 and PA12. It has been reported that a surface containing carboxylic acid groups could coordinatively bind metal cations in solution phase, and could help the nucleation and crystal growth of MOFs [31,32]. In our study, it is possible that the terminal carboxylate group on the surface of PA12 particle interacts with the $Co^{2+}$ ions in the solvent, and initiate the nucleation and growth of ZIF-67. This proposed formation mechanism of ZIF-67 could explain the above TGA and AFM results.

TGA test was also used to determine the real weight of ZIF-67 in the prepared ZIF67-PA12 powders. Based on the residual weight percentage at 750 °C, the TGA tests revealed a measured 2.6 wt% ZIF-67 content on the theoretically determined 2 wt% ZIF67-PA12 powder (through the synthesis process). In the case of the theoretically determined 1 wt% content of ZIF67 in ZIF67-PA12, the TGA results had a measured value of 1.4 wt% ZIF67 in ZIF67-PA12 and for the 0.1 wt% ZIF-67, the TGA data revealed a similar measured wt%.

Powder flowability is an important factor of laser sintering. The

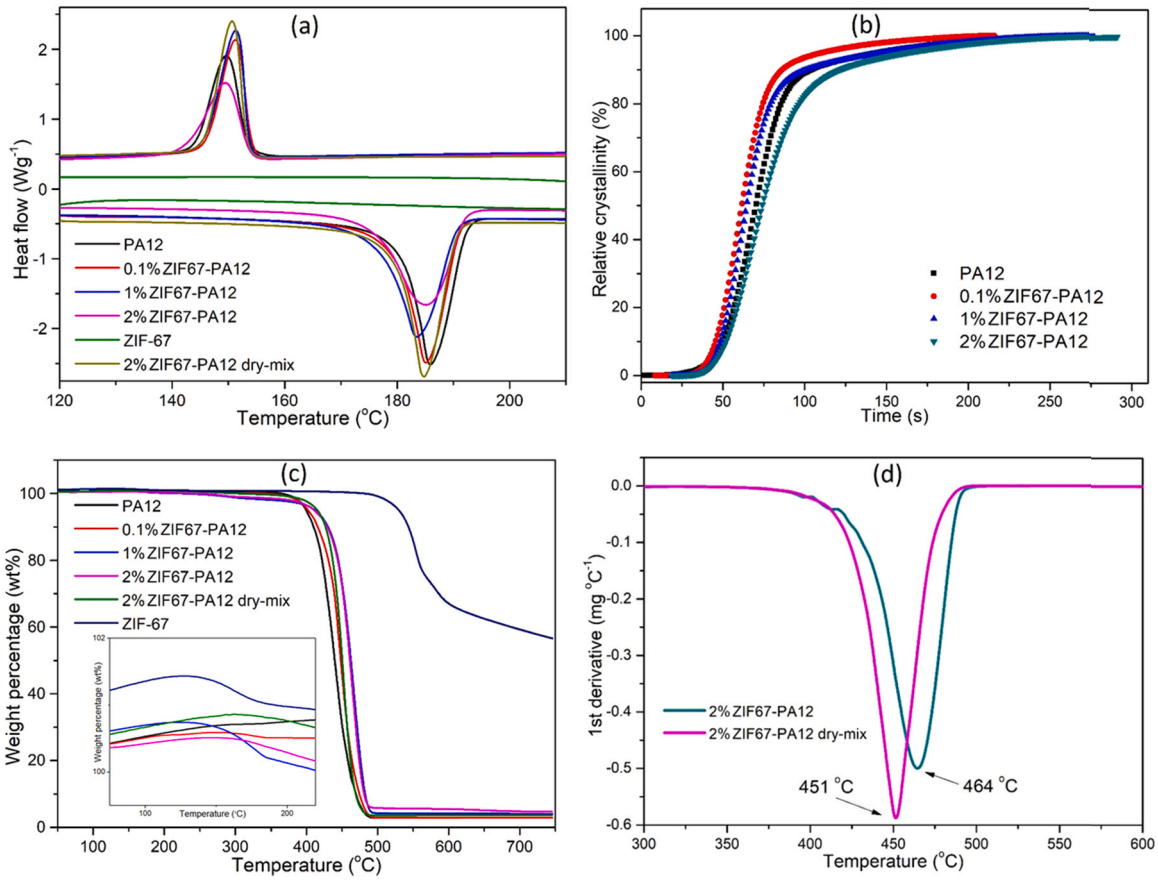


**Fig. 6.** (a) DSC curves of endothermic and exothermic phase changes during a heating and cooling cycle at 10 °C min$^{-1}$ for plain PA12 and ZIF67-PA12 powders, showing the shifted melting and crystallisation peaks under various amounts of ZIF-67 crystals; (b) Relative crystallinity vs time of plain PA12 and ZIF67-PA12 powders, showing the effect of ZIF-67 on the rate of PA12 crystallization; (c) TGA curves of plain PA12 and ZIF67-PA12 powders, inset is the zoomed in image; (d) the 1st derivative of a TGA thermograms for 2%ZIF67-PA12 and 2%ZIF67-PA12 dry-mix powder, showing a 13 °C difference in the degradation point.

**Table 2**
DSC and TGA results for PA and ZIF67-PA12 powders.

| Material | $T_m$ (°C) | $T_{m\ onset}$ (°C) | $T_c$ (°C) | $T_{c\ onset}$ (°C) | $T_{deg}$ (°C) | Residual weight (%) |
|---|---|---|---|---|---|---|
| PA12 | 185.77 | 180.78 | 149.76 | 153.54 | 442 | 2.91 |
| 0.1% ZIF67-PA12 | 185.03 | 179.68 | 151.32 | 154.24 | 446 | 2.94 |
| 1%ZIF67-PA12 | 183.52 | 177.43 | 151.47 | 153.80 | 460 | 3.67 |
| 2%ZIF67-PA12 | 184.94 | 175.11 | 149.51 | 153.81 | 464 | 4.31 |

$T_m$ is melting temperature; $T_{m\ onset}$ is onset melting temperature; $T_c$ is crystallisation temperature and $T_{c\ onset}$ is onset crystallisation temperature; $T_{deg}$ is thermal degradation temperature.

**Table 3**
Powder rheology results of plain PA12 and ZIF67-PA12 powders.

| Material | Basis Flow Energy (BFE) (mJ) | Stability Index (SI) | Specific Energy (SE) (mJ/g) | Conditioned Bulk Density (CBD) (g/ml) |
|---|---|---|---|---|
| PA12 | 208.18 ± 3.85 | 0.93 ± 0.03 | 6.61 ± 0.12 | 0.47 ± 0.001 |
| 0.1% ZIF67-PA12 | 146.29 ± 4.52 | 0.95 ± 0.04 | 5.11 ± 0.21 | 0.46 ± 0.001 |
| 1% ZIF67-PA12 | 124.03 ± 0.54 | 0.94 ± 0.02 | 3.89 ± 0.02 | 0.49 ± 0.001 |
| 2% ZIF67-PA12 | 118.64 ± 4.04 | 0.93 ± 0.01 | 3.50 ± 0.06 | 0.53 ± 0.004 |

powder flow characteristics of the in-situ synthesised ZIF67-PA12 were measured and listed in Table 3. The plain PA12 had been tested for comparison purposes. The plain PA12 has the highest Basic Flow Energy (BFE) value of 208.18 mJ among all the powders, suggesting that it needs the highest energy to displace the powder in a confined environment under rotation. The addition of ZIF-67 crystals on the PA12 particle surface decreases the BFE value from 146.29 mJ of 0.1%ZIF67-PA12 to 118.64 mJ of 2%ZIF67-PA12. This means ZIF-67 coating is beneficial to decrease energy for the displacement of powders. The SE values have the similar trend to BFE values. Plain PA12 requires energy of 6.61 mJ/g to lift the particles in a low-stress environment; while 0.1% ZIF67-PA12, 1%ZIF67-PA12, and 2%ZIF67-PA12 needs less energy of 5.11, 3.89 and 3.50 mJ/g, respectively. Both the decrease of values of BFE and SE can be attributed to the surface change of the ZIF67-PA12 particles. As ZIF-67 has been reported to have a promising anti-wear property, the presence of ZIF-67 is helpful to reduce the powder flow energy [33].

It can be noticed that there is a slight increase of Conditioned Bulk Density (CBD) value with the increase of ZIF-67 amount, which means that 2%ZIF67-PA12 has a higher packing density. The bulk density of ZIF-67 is about 0.35 g/cm$^3$, it is possible that the presence of ZIF-67 on the surface increase the density of the particles and it allows better compaction of the powder as well. The CBD values also indicate that the particle sizes amongst the powder grades remained similar, which is consistent with the PSD results. The stability index (SI) shows no change

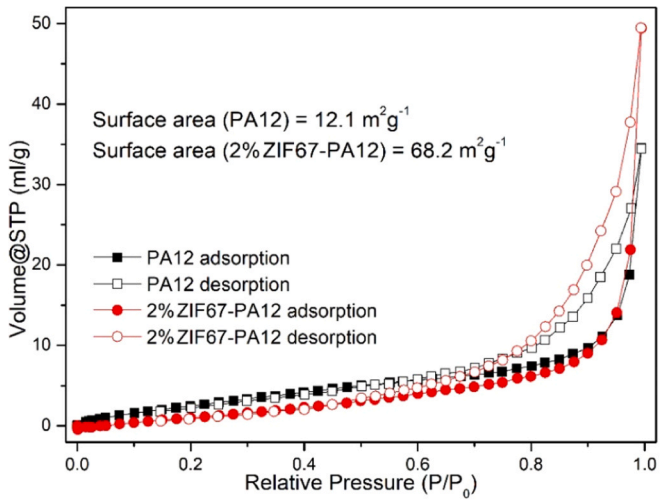


**Fig. 7.** Nitrogen sorption isotherms for plain PA12 powder and 2%ZIF67-PA12 powder.

amongst the four powders, a sign that the tested powders are stable and can be repeatedly used.

The textural properties of ZIF67-PA12 composite powders were obtained from nitrogen adsorption–desorption measurement. As shown in Fig. 7, the nitrogen sorption of plain PA12 powder is lower than that of ZIF67-PA12 composite powders. All powders show that their adsorption and desorption branches are reversible with a hysteresis loop, indicating the presence of particle gaps or voids within the powders. The presence of ZIF-67 crystals on the surface of PA12 particles increases the surface area of the ZIF67-PA12 powders from a value of 12.1 for PA12 powder to 68.2 $m^2/g$ in the case of 2%ZIF67-PA12. PA12 powder is non-porous therefore its surface area is low; while ZIF-67 crystal is a nano-porous material with a surface area of 1600 $m^2/g$ (shown in Fig. S4 and S5).

### 3.2. Characterisation of laser-sintered parts

The as-printed solid and porous lattice structure are presented in Fig. 8. The colour of both as-printed parts is purple, due to the presence

**Table 4**
Comparison of designed and measured dimension of the 2%ZIF67-PA12 solid part presented in Fig. 1c.

| | X (mm) | Y (mm) | Z (mm) |
|---|---|---|---|
| Designed | 5 | 5 | 5 |
| Measured Sample No. 1 | 5.29 ± 0.02 | 5.24 ± 0.08 | 5.24 ± 0.02 |
| Measured Sample No. 2 | 5.24 ± 0.03 | 5.34 ± 0.03 | 5.19 ± 0.03 |

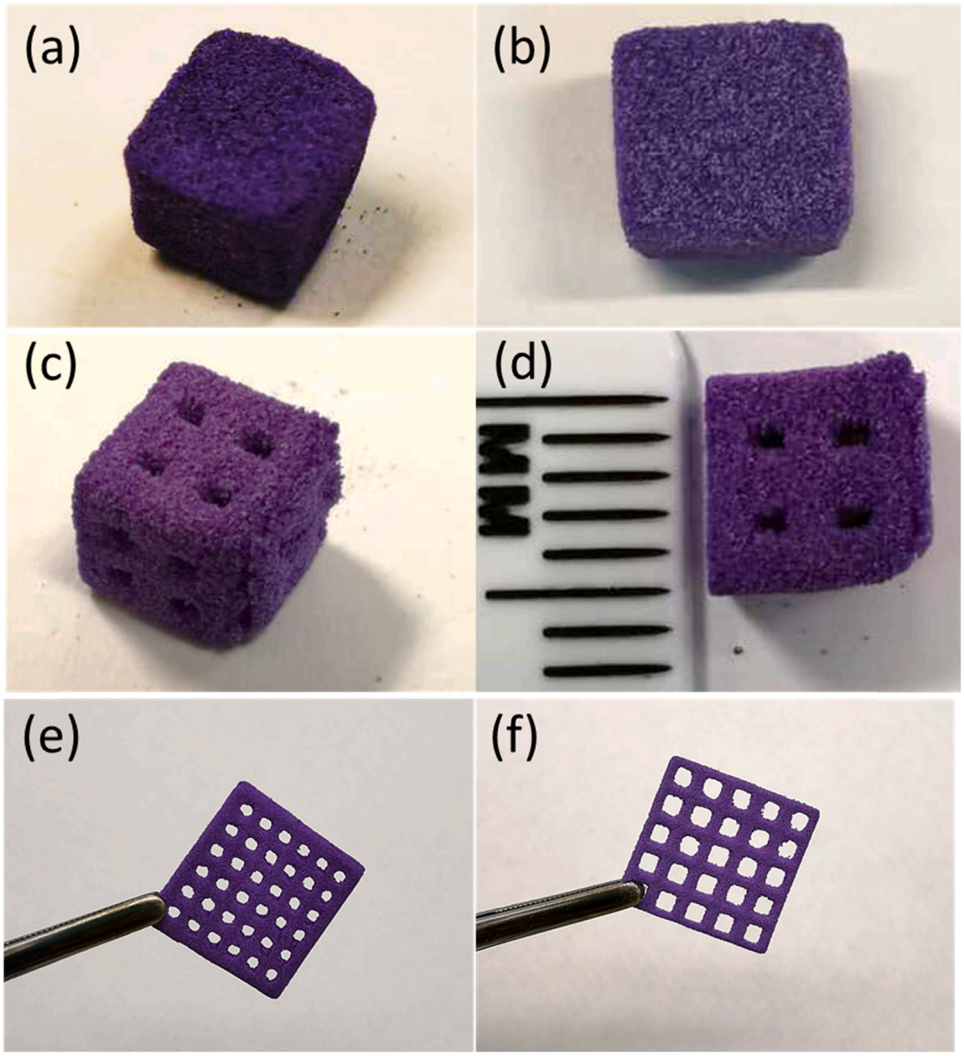


**Fig. 8.** The as printed (a-b) solid, (c-d) porous lattice structure, and (e-f) other mesh-like structures.

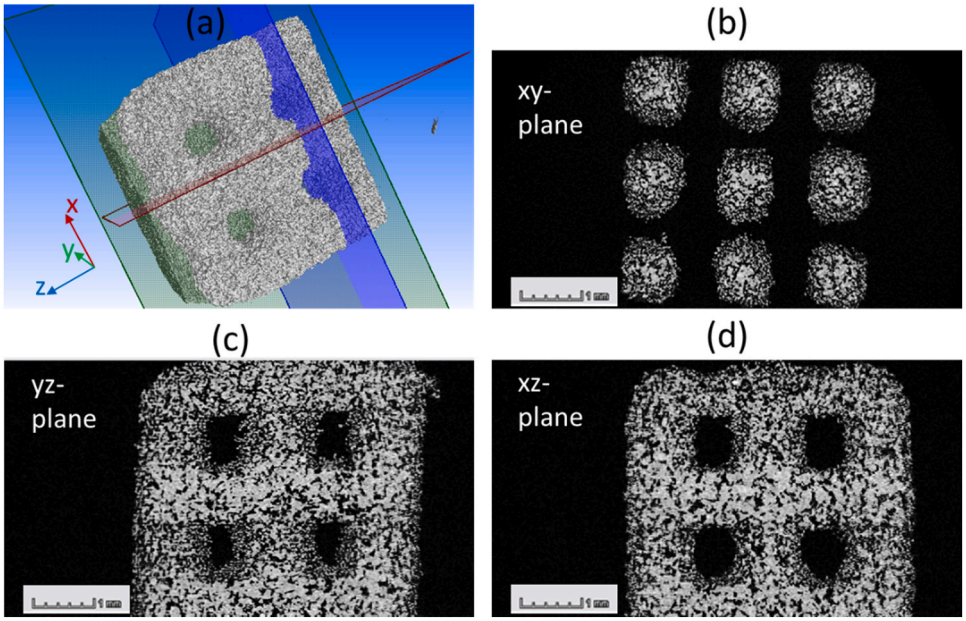


**Fig. 9.** (a) Micro-CT 3D image of 2%ZIF-67-PA12 porous part, and its 2D image view in (b) xy-plane, (c) yz-plane, (d) zx-plane.

of ZIF-67. The as-printed parts have recorded some level of distortion when compared with the CAD design (shown in Fig. 1). It was found that the printed part is bigger in size by a range of 0.19–0.34 mm. The results are presented in Table 4. In addition, other mesh-like structures, only three-layer thick, were also successfully fabricated and are shown in Fig. 8e and f. The size of the mesh is 20 mm * 20 mm * 0.3 mm with uniformly distributed square holes in the dimensions of 2 mm * 2 mm and 3 mm * 3 mm. These additional structures shown in Fig. 8e and f are used here only for demonstration, the solid and porous cubes were used for further characterisation and testing.

Micro-CT was employed to investigate the 3D structure of 2%ZIF67-PA12 porous part. Fig. 9a shows the 3D reconstruction of the 2%ZIF67-PA12 porous part, and Fig. 9b to d shows its 2D image view in xy-plane, yz-plane, and zx-plane, respectively. In the 2D images, the black areas represent pores in the structure, while the bright areas represent the dense part of the structure, including PA12 and ZIF-67. The designed large cubic built within the structure with connected channels are clearly shown in these 2D images. In addition, the small black dots shown in Fig. 9b to d suggest the presence of small pores through the part. The zoomed in CT images (shown in Fig. S6 and S7) also support the presence of small pores through the 2%ZIF67-PA12 porous part. As a result, these macropores from the structure and micropores from ZIF-67 crystals both contribute the hierarchical porous lattice structure.

The 2%ZIF67-PA12 porous structures was also examined by SEM presented in Fig. 10. The surface of the printed part in the vicinity of the pore area is shown in Fig. 10a and high magnification regions of the printed surface, clearly showing the presence of ZIF-67 across the surface, are included in Fig. 10b and c. In addition, the energy-dispersive X-ray spectroscopy of 2%ZIF-67-PA12 porous part shows a good dispersion of the ZIF-67 crystals (Fig. 10d and e). The reason for such a good coverage of the printed part with ZIF-67 lays within the in-situ synthesis process combined with the powder bed fusion process itself. At the end of the printing process, the final printed layers (in a semi-molten state) get covered with fresh layers of powder hence the printed part ends up with a layer of semi sintered particles which gives the part the well-known rough surface finish with ZIF-67 exposure.

The powder bed process employed a $CO_2$ laser, known to allow a good absorption of polymeric materials such as PA12. From the literature [26], it has been reported that the FTIR in-plane bending vibrations and stretching vibrations of the imidazole rings in ZIF-67 are present at approx. 1000 $cm^{-1}$ wavenumbers, which is well within the radiation band of the $CO_2$ laser, indicating that ZIF-67 can be effectively absorb the $CO_2$ laser energy [26]. Fracture surface SEM images revealed a combination of ductile regions and some porous areas (see Fig. S8).

The mechanical performance of PA12 solid part and 2%ZIF67-PA12 solid part was evaluated through a compression test. As can be seen in Fig. 11, the addition of ZIF-67 leads to a big reduction in stress from approx. 95 MPa to 30 Mpa when compared to the plain PA12. Fig. 11 inset shows the compressed structures of both parts after the test, where the compressed 2%ZIF67-PA12 solid part has a more disorder structure than PA12. The possible reason could be that the addition of ZIF-67 changed the polymer melt flow characteristics, and slowed down the particle coalescence, further weaken the particle-particle bonding. However, this issue can be solved by increasing the energy density. The intension here is not to optimise the mechanical performance but to show that the powder bed fusion process can be used as a manufacturing process to build up a hierarchical structure scaffold for MOFs, which will ultimately allow to use MOFs in a wider range of applications.

MOFs can act as solid adsorbents for $CO_2$ capture due to their high porosity and rich functionality [34,35]. For this reason, the $CO_2$ capacity of the ZIF67-PA12 laser sintered parts was tested, and the results are summarised in Fig. 12 and Table 5. The $CO_2$ adsorption performance from the literature was also compared in Table 5. The data confirms that by designing a part with increased surface area through the addition of the lattice structure, the number of ZIF-67 active sites are increased, and thus the $CO_2$ absorption is significantly improved. To the best of our knowledge, there is only one paper available presenting the laser-sintering of MOF-polymer composite powders for $CO_2$ adsorption. 10 wt% MOF (HKUST-1)-PA12 dry-mixed powders were laser sintered as solid disks (MOF/N12) with a $CO_2$ capacity of 3.05 $cm^3/g$ at 298 K and 1 bar [25].

Apart from using laser sintering technology, other methods were used from the literature to fabricate simple structures for $CO_2$ adsorption. Hong et al. reported that they used by a paste extrusion technique to fabricate a MIL-101 (Cr) monolith using bentonite clay as a binder, where the weight percentage of MIL101 (Cr) is as high as 75%. Its maximum $CO_2$ capacity is 11.2 $cm^3/g$ at 298 K and 1 bar (Table 5) [36]. Chang et al. applied a wet granulation method to prepare millimetre-scale spheres of MIL-101 (Cr) and UiO-66 (Zr), using mesoporous γ-alumina as a binder [37]. The weight percentage of MOFs is as

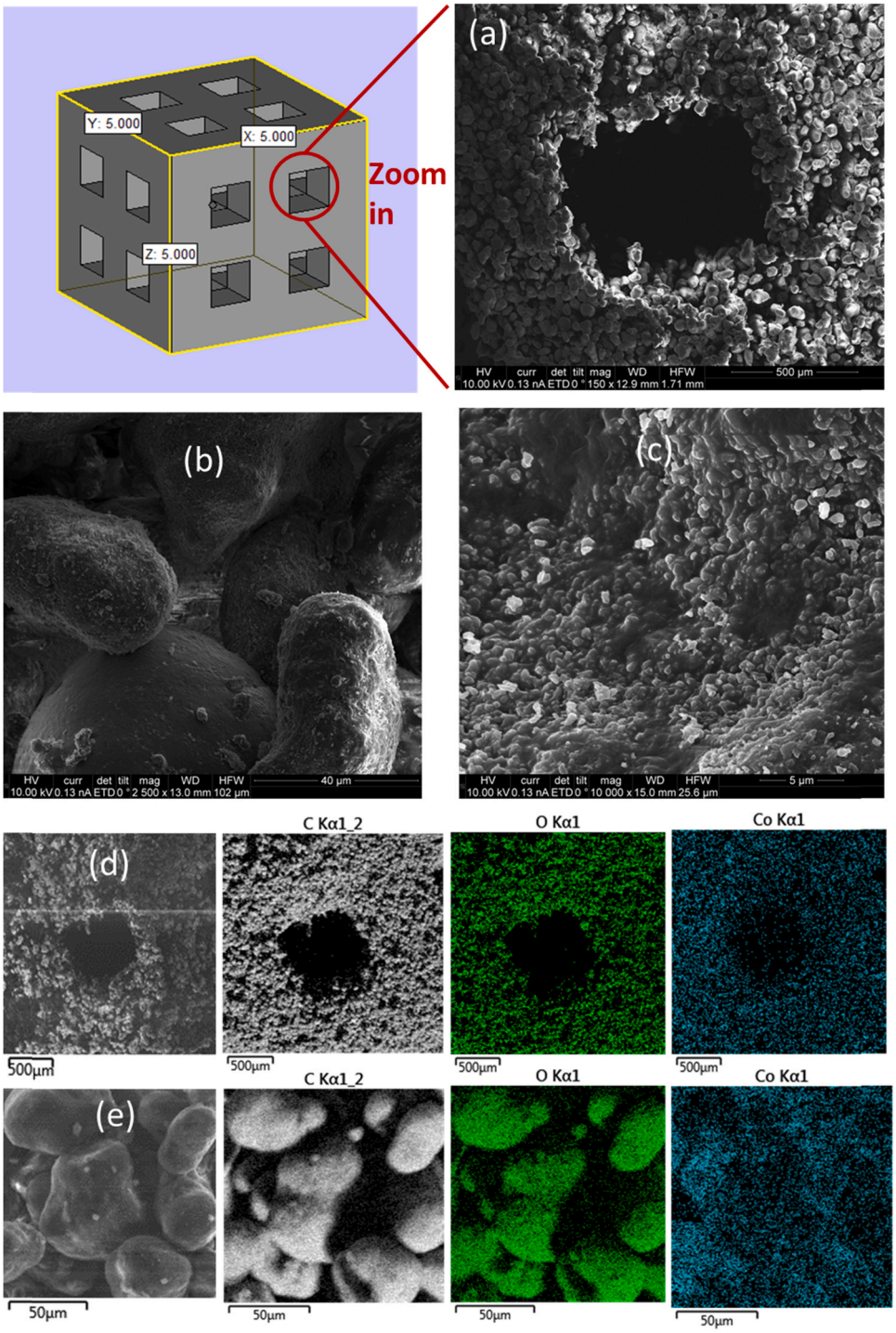


**Fig. 10.** SEM images of 2%ZIF67-PA12 laser-sintered porous part under (a-b) low and (c) high magnification, and (d-e) their corresponding energy-dispersive X-ray spectroscopy. Figs. 10c-e show that the ZIF-67 crystals are well dispersed and exposed on the surface of the laser-sintered part.

high as 95%. The maximum $CO_2$ capacity at 298 K and 1 bar can be achieved to 60 and 25 $cm^3/g$, respectively. However, these two methods mentioned above cannot fabricate complex structure using laser sintering.

### 3.3. Double coating process

In general, a higher ZIF-67 content in a composite powder results in a higher $CO_2$ capacity. For this in-situ method of fabrication of powders and manufacture of printed parts, higher concentrations of ZIF-67 were also explored. A 5 wt% ZIF67-PA12 powder was also prepared but its spreadability and processability within the powder bed was extremely poor and had to be abandoned. However, in an attempt to increase further the amount of ZIF-67 crystals available on the surface, a dip coating method was applied. The laser sintered 2%ZIF67-PA12 porous part was dipped in the ZIF-67 precursor solution and allowed to form further crystals. The SEM images in Fig. 13 shows that a second layer of ZIF-67 crystals was formed on the surface of the printed part already presenting a layer of ZIF-67 crystals.

In spite of an increased number of crystal sites, surprisingly, the $CO_2$

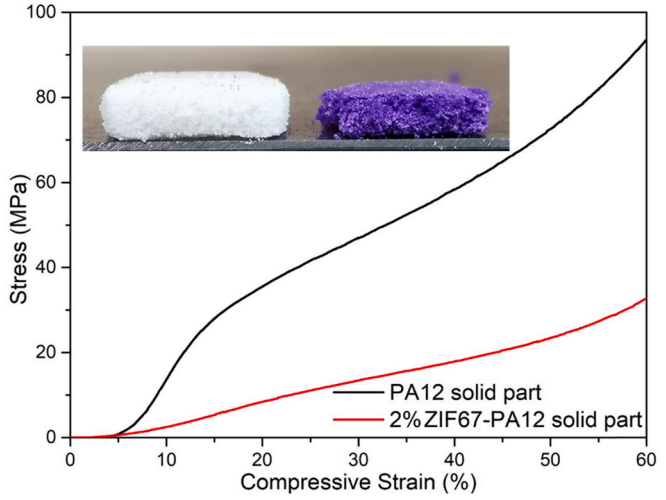


**Fig. 11.** Compressive Strain-Stress curves of PA12 solid part and 2%ZIF67-PA12 solid part. Inset is the digital image of PA12 solid part (white colour) and 2%ZIF67-PA12 solid part (purple colour) after the compression test.

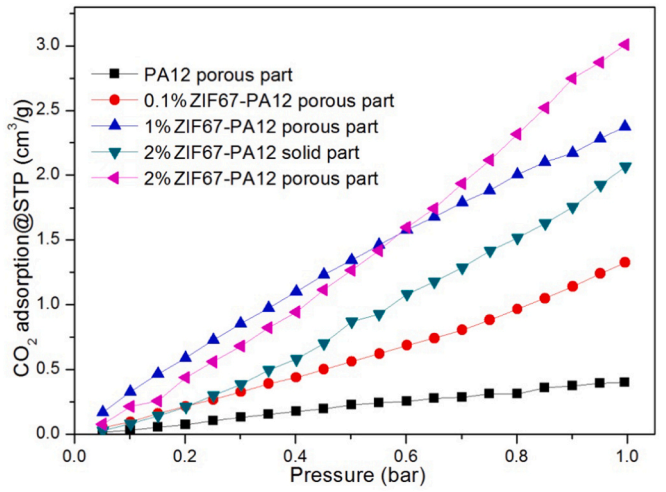


**Fig. 12.** $CO_2$ adsorption capacities at 298 K for sample PA12 porous part, 0.1% ZIF67-PA12 porous part, 1%ZIF67-PA12 porous part, 2%ZIF67-PA12 solid part and 2%ZIF67-PA12 porous part.

capacity value of the dipped part at 298 K at 1 bar was only 2.76. At this stage, it is not clear why this value was not significantly higher as expected. This could be due to the blockage of the active sites in the first ZIF-67 layer, which resulted in exposure of more or less the same surface area but this time in the second layer, therefore maintaining the same $CO_2$ capacity. As it can be seen in Figs. 10 and 13, the first layer of ZIF-67 built in through the in-situ hydrothermal synthesis straight onto the polymeric particles has the advantage of having the ZIF-67 crystals partially embedded in the polymer structure, hence giving the structure the necessary robustness and ease to use. It is not clear how well the second layer is attached and whether would be easy to handle as a structure. Further research is required to understand the benefits of the second layer, its optimisation and even addition of a different type of MOFs as the second layer.

## 4. Conclusions and outlook

An in-situ hydrothermal synthesis method has been successfully applied on the formation of ZIF67-PA12 nanocomposite powder, where ZIF-67 crystals grow on the surface of PA12 polymeric particle. A series

**Table 5**
Comparison of $CO_2$ adsorption performance between this study and literature.

| Material | Fabrication method | Maximum $CO_2$ capacity ($cm^3\ g^{-1}$) | | Reference |
|---|---|---|---|---|
| | | 298 K at 1 bar | 273 K at 1 bar | |
| ZIF-67 powder | N/A | 20.1 | 32.3 | This study |
| PA12 porous part | Laser sintering | 0.40 | 0.97 | This study |
| 2%ZIF67-PA12 porous part | Laser sintering | 3.02 | 4.89 | This study |
| 2%ZIF67-PA12 solid part | Laser sintering | 2.08 | 2.81 | This study |
| MOF/N12 disk (10 wt % HKUST-1/PA12) | Laser sintering | 3.05 | N/A | [25] |
| MIL-101 (Cr) monolith (75 wt% of MIL-101) | Paste extrusion technique | ~ 11.2 | N/A | [36] |
| MIL-101 (Cr) spheres (95 wt% of MIL-101) | Wet granulation method | ~ 60 | N/A | [37] |
| UiO-66 (Zr) spheres (95 wt% of UiO-66) | Wet granulation method | ~ 25 | N/A | [37] |

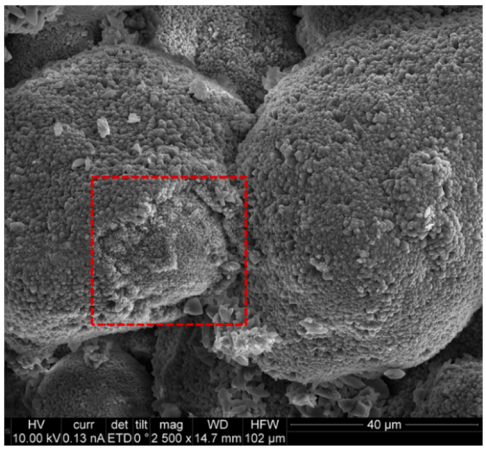


**Fig. 13.** SEM image of the surface of double-coated 2%ZIF67-PA12 porous part. The highlight the region illustrates the first and second ZIF-67 layer.

of characterisation techniques including particle size distribution, powder rheology test and thermal analysis were measured and confirmed the processibility of ZIF67-PA12 powders for powder bed fusion process. Among the laser sintered parts, 2%ZIF67-PA12 porous part exhibited the highest $CO_2$ capacity of 3.02 and 4.89 $cm^3/g$ at 298 K and 273 K at 1 bar, respectively. This high $CO_2$ adsorption performance could be due to: a good dispersion of ZIF-67 crystals throughout the polymer matrix by using in-situ synthesis method; and sufficient exposed ZIF-67 sites for $CO_2$ adsorption by using the design of a porous lattice laser-sintered structure.

The ability to easily laser sinter MOFs composite powders into complex structures will speed up the adoption of MOFs in existing and new applications. MOFs are used for holding toxic gases into gas storage cylinders, such as NuMat's ION-X cylinders [38] and are being looked at for a wide range of other applications [39]. One can imagine fabrication of complex lattice structures of controlled pore shapes and sizes, or films with well define surface features to enhance even further the unique properties of MOFs – all possible through laser sintering. For example, TPU laser sintering is currently used for fabrication of custom shoe soles for comfort and flexibility [40]. MOF-TPU powders, with MOFs acting as a source of antimicrobial agent could create the ideal insoles structure for medical and sports footwear. MOF-polymer knitted textiles could

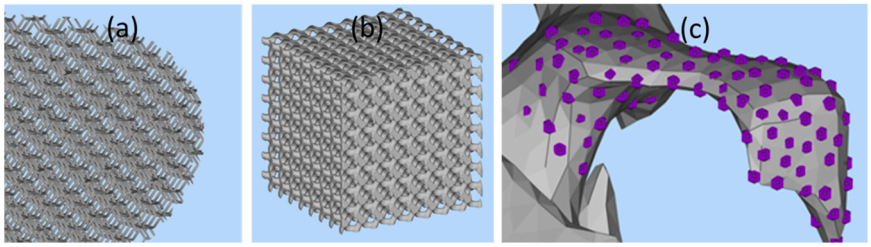


**Fig. 14.** (a) Fan blade tip with a super fine mesh pattern; (b) gyroid structure suitable for air or liquid filtration (c) zoom in image of gyroid cell with MOFs embedded onto the surface (purple structures represent the MOFs).

also form the framework for specialist medical garments. Laser sintered filters with a continuous release of antibacterial, delivered through the MOFs present on the surface, could improve the air quality in air management system of building. A porous MOF-polymer structure (shown in Fig. 14a) could be built into the blades of air ventilation fans of vacuum cleaners or computers and similarly help maintain a cleaner air. The example gyroid design in Figs. 14b and c, known to have a high surface area to volume ratio, could be used to laser sinter filters of various sizes, shapes and pores.

## 5. CRediT authorship contribution statement

**Binling Chen:** Writing- Original Draft, Conceptualisation, Methodology, Investigation. **Richard Davies:** Writing- Reviewing and Editing, Validation, Methodology. **Hong Chang:** Methodology. **Yongde Xia:** Writing- Reviewing and Editing. **Yanqiu Zhu:** Writing- Reviewing and Editing. **Oana Ghita:** Writing- Reviewing and Editing, Supervision, Funding acquisition.

## Declaration of Competing Interest

The authors declare that they have no known competing financial interests or personal relationships that could have appeared to influence the work reported in this paper.

## Acknowledgements

The authors would like to thank the UK Engineering and Physical Science Research Council for its funding (EPSRC grant - Novel high performance polymeric composite materials for additive manufacturing of multifunctional components EP/N034627/1), Dr Vishal Panchal and Stephen Lewandowski for their kind help with the AFM measurement.

## Appendix A. Supporting information

Supplementary data associated with this article can be found in the online version at doi:10.1016/j.addma.2020.101774.

## References

[1] S.C. Ligon, R. Liska, J. Stampfl, M. Gurr, R. Mülhaupt, Polymers for 3D printing and customized additive manufacturing, Chem. Rev. 117 (2017) 10212–10290.
[2] J. Bai, S. Yuan, F. Shen, B. Zhang, C.K. Chua, K. Zhou, J. Wei, Toughening of polyamide 11 with carbon nanotubes for additive manufacturing, Virtual Phys. Prototyp. 12 (2017) 235–240.
[3] Y. Wang, D. Rouholamin, R. Davies, O.R. Ghita, Powder characteristics, microstructure and properties of graphite platelet reinforced Poly Ether Ether Ketone composites in High Temperature Laser Sintering (HT-LS), Mater. Des. 88 (2015) 1310–1320.
[4] S. Yuan, F. Shen, C.K. Chua, K. Zhou, Polymeric composites for powder-based additive manufacturing: materials and applications, Prog. Polym. Sci. 91 (2019) 141–168.
[5] W. Zhu, C. Yan, Y. Shi, S. Wen, J. Liu, Q. Wei, Y. Shi, A novel method based on selective laser sintering for preparing high-performance carbon fibres/polyamide12/epoxy ternary composites, Sci. Rep. 6 (2016) 33780.
[6] M. Yan, X. Tian, G. Peng, D. Li, X. Zhang, High temperature rheological behavior and sintering kinetics of CF/PEEK composites during selective laser sintering, Compos. Sci. Technol. 165 (2018) 140–147.
[7] H. Thakkar, S. Eastman, A. Hajari, A.A. Rownaghi, J.C. Knox, F. Rezaei, 3D-printed zeolite monoliths for $CO_2$ removal from enclosed environments, ACS Appl. Mater. Interfaces 8 (2016) 27753–27761.
[8] G.J.H. Lim, Y. Wu, B.B. Shah, J.J. Koh, C.K. Liu, D. Zhao, A.K. Cheetham, J. Wang, J. Ding, 3D-printing of pure metal–organic framework monoliths, ACS, Mater. Lett. 1 (2019) 147–153.
[9] D. Vak, K. Hwang, A. Faulks, Y.-S. Jung, N. Clark, D.-Y. Kim, G.J. Wilson, S. E. Watkins, 3D printer based slot-die coater as a lab-to-fab translation tool for solution-processed solar cells, Adv. Energy Mater. 5 (2015), 1401539.
[10] A. Zhakeyev, P. Wang, L. Zhang, W. Shu, H. Wang, J. Xuan, Additive manufacturing: unlocking the evolution of energy materials, Adv. Sci. 4 (2017), 1700187.
[11] C. Zhu, T. Liu, F. Qian, W. Chen, S. Chandrasekaran, B. Yao, Y. Song, E.B. Duoss, J. D. Kuntz, C.M. Spadaccini, M.A. Worsley, Y. Li, 3D printed functional nanomaterials for electrochemical energy storage, Nano Today 15 (2017) 107–120.
[12] A.E. Baumann, D.A. Burns, B. Liu, V.S. Thoi, Metal-organic framework functionalization and design strategies for advanced electrochemical energy storage devices, Commun. Chem. 2 (2019) 86.
[13] S. Yuan, Y. Zheng, C.K. Chua, Q. Yan, K. Zhou, Electrical and thermal conductivities of MWCNT/polymer composites fabricated by selective laser sintering, Compos. Part A Appl. Sci. Manuf. 105 (2018) 203–213.
[14] S. Yuan, C.K. Chua, K. Zhou, 3D-printed mechanical metamaterials with high energy absorption, Adv. Mater. Technol. 4 (2019), 1800419.
[15] L.J. Tan, W. Zhu, K. Zhou, Recent Progress on Polymer Materials for Additive Manufacturing, Adv. Funct. Mater., n/a 2003062.
[16] L.J. Tan, W. Zhu, K. Zhou, Development of organically modified montmorillonite/polypropylene composite powders for selective laser sintering, Powder Technol. 369 (2020) 25–37.
[17] H.-C. Zhou, J.R. Long, O.M. Yaghi, Introduction to metal–organic frameworks, Chem. Rev. 112 (2012) 673–674.
[18] H. Furukawa, K.E. Cordova, M. O'Keeffe, O.M. Yaghi, The chemistry and applications of metal-organic frameworks, Science 341 (2013), 1230444.
[19] B. Chen, Z. Yang, Y. Zhu, Y. Xia, Zeolitic imidazolate framework materials: recent progress in synthesis and applications, J. Mater. Chem. A 2 (2014) 16811–16831.
[20] G. Zhong, D. Liu, J. Zhang, The application of ZIF-67 and its derivatives: adsorption, separation, electrochemistry and catalysts, J. Mater. Chem. A 6 (2018) 1887–1899.
[21] M.C. Kreider, M. Sefa, J.A. Fedchak, J. Scherschligt, M. Bible, B. Natarajan, N. N. Klimov, A.E. Miller, Z. Ahmed, M.R. Hartings, Toward 3D printed hydrogen storage materials made with ABS-MOF composites, Polym. Adv. Technol. 29 (2018) 867–873.
[22] M.S. Michael Bible, James A. Fedchak, Julia Scherschligt, Bharath Natarajan, Zeeshan Ahmed, Matthew R. Hartings, 3D-printed acrylonitrile butadiene styrene-metal organic framework composite materials and their gas storage properties, 3D print, Addit. Manuf. 5 (2018) 63–72.
[23] A.J. Young, R. Guillet-Nicolas, E.S. Marshall, F. Kleitz, A.J. Goodhand, L.B. L. Glanville, M.R. Reithofer, J.M. Chin, Direct ink writing of catalytically active UiO-66 polymer composites, Chem. Commun. 55 (2019) 2190–2193.
[24] Z. Lyu, G.J.H. Lim, R. Guo, Z. Kou, T. Wang, C. Guan, J. Ding, W. Chen, J. Wang, 3D-printed MOF-derived hierarchically porous frameworks for practical high-energy density Li–O2 batteries, Adv. Funct. Mater. 29 (2019), 1806658.
[25] E. Lahtinen, R.L.M. Precker, M. Lahtinen, E. Hey-Hawkins, M. Haukka, Selective laser sintering of metal-organic frameworks: production of highly porous filters by 3D printing onto a polymeric matrix, ChemPlusChem 84 (2019) 222–225.
[26] R. Li, S. Yuan, W. Zhang, H. Zheng, W. Zhu, B. Li, M. Zhou, A. Wing-Keung Law, K. Zhou, 3D printing of mixed matrix films based on metal–organic frameworks and thermoplastic polyamide 12 by selective laser sintering for water applications, ACS Appl. Mater. Interfaces 11 (2019) 40564–40574.
[27] M. Wang, J. Liu, C. Guo, X. Gao, C. Gong, Y. Wang, B. Liu, X. Li, G.G. Gurzadyan, L. Sun, Metal–organic frameworks (ZIF-67) as efficient cocatalysts for photocatalytic reduction of $CO_2$: the role of the morphology effect, J. Mater. Chem. A 6 (2018) 4768–4775.
[28] J. Qian, F. Sun, L. Qin, Hydrothermal synthesis of zeolitic imidazolate framework-67 (ZIF-67) nanocrystals, Mater. Lett. 82 (2012) 220–223.

[29] J. Yao, M. He, K. Wang, R. Chen, Z. Zhong, H. Wang, High-yield synthesis of zeolitic imidazolate frameworks from stoichiometric metal and ligand precursor aqueous solutions at room temperature, CrystEngComm 15 (2013) 3601–3606.
[30] S. Berretta, K.E. Evans, O.R. Ghita, Predicting processing parameters in high temperature laser sintering (HT-LS) from powder properties, Mater. Des. 105 (2016) 301–314.
[31] M.T. Conato, A.J. Jacobson, Control of nucleation and crystal growth kinetics of MOF-5 on functionalized gold surfaces, Microporous Mesoporous Mater. 175 (2013) 107–115.
[32] L. Hou, M. Zhou, X. Dong, L. Wang, Z. Xie, D. Dong, N. Zhang, Controlled growth of metal-organic frameworks on polymer brushes, Chem. Eur. J. 23 (2017) 13337–13341.
[33] Q. Shi, Z. Chen, Z. Song, J. Li, J. Dong, Synthesis of ZIF-8 and ZIF-67 by steam-assisted conversion and an investigation of their tribological behaviors, Angew. Chem. Int. Ed. 50 (2011) 672–675.
[34] Z. Hu, Y. Wang, B.B. Shah, D. Zhao, $CO_2$ capture in metal–organic framework adsorbents: an engineering, Adv. Sustain. Syst. 3 (2019), 1800080.
[35] K. Sumida, D.L. Rogow, J.A. Mason, T.M. McDonald, E.D. Bloch, Z.R. Herm, T.-H. Bae, J.R. Long, Carbon dioxide capture in metal–organic frameworks, Chem. Rev. 112 (2012) 724–781.
[36] W.Y. Hong, S.P. Perera, A.D. Burrows, Manufacturing of metal-organic framework monoliths and their application in $CO_2$ adsorption, Microporous Mesoporous Mat. 214 (2015) 149–155.
[37] A.H. Valekar, K.-H. Cho, U.H. Lee, J.S. Lee, J.W. Yoon, Y.K. Hwang, S.G. Lee, S. J. Cho, J.-S. Chang, Shaping of porous metal–organic framework granules using mesoporous ρ-alumina as a binder, RSC Adv. 7 (2017) 55767–55777.
[38] N. Technologies, ⟨https://www.numat-tech.com/ion-x/⟩, 2020.
[39] N. Notman, MOFs find a use, Chem. World (2017).
[40] EOS, Comfortable 3D Printing Solutions for Shoe Manufacturers and Their Customers, 2020.